https://doi.org/10.1016/j.cej.2021.132615

A Rational Design of FeNi Alloy Nanoparticles and Carbonate-Decorated Perovskite as a Highly Active and Coke-resistant Anode for Solid Oxide Fuel Cells

Shuo Zhai[1, 2, 3], Heping Xie[1, 3*], Bin Chen[1, 2*], Meng Ni[2]

[1]Guangdong Provincial Key Laboratory of Deep Earth Sciences and Geothermal Energy Exploitation and Utilization, Institute of Deep Earth Sciences and Green Energy, Shenzhen University, Shenzhen 518060, China.

[2]Building Energy Research Group, Department of Building and Real Estate, The Hong Kong Polytechnic University, Hung Hom, Kowloon, Hong Kong, China.

[3]Institute of New Energy and Low-Carbon Technology, Sichuan University, Chengdu 610065, China.

***Corresponding authors**

Email addresses: xiehp@scu.edu.cn; chenbin@szu.edu.cn

Abstract

Solid oxide fuel cells (SOFCs) are a kind of clean and efficient device to convert chemical energy in fuels into electricity. However, since anodes with high catalytic activity and carbon tolerance are still underdeveloped, the consequent serious performance degradation of the cells under operational conditions significantly confines their commercial applications. Here we propose a new strategy to remove carbon deposition by in-situ formation of alkali metal carbonate on the anode surface. A multi-phase composite anode, which is composed of an orthorhombic single perovskite main phase, a Ruddlesden-Popper (RP) layered perovskite second phase, and an in-situ exsolved FeNi alloy minor phase, is developed by one-step reduction of $La_{0.65}Li_{0.05}Sr_{0.3}Fe_{0.8}Ni_{0.2}O_{3-\delta}$ ($LLSFN_{0.05}$) at a high temperature. The deficiencies of the RP phase and A-site caused by Li dopant would increase oxygen bulk diffusion, and FeNi nanoparticles would boost the catalytic activity. Moreover, when dealing with carbon fuel, lithium carbonate can be synthesized on the anode surface, serving as a good oxygen ion conductor and an efficient catalyst for coke removal by gasification. A single cell with our reduced $LLSFN_{0.05}$ anode exhibited maximum power densities of 596, 467, and 424 mW cm^{-2} at 750 °C with H_2, CO, and wet C_2H_6 as the fuel, respectively. In addition, the cells could have a long-term stable operation for over 80 h using CO as the fuel at 200 mA cm^{-2}. This study provides a new material design strategy to develop a highly active and coke-resistant anode.

Keywords:

Solid oxide fuel cell, perovskite, anode, nanoparticle exsolution, carbonate

1. Introduction

As a promising clean energy technology, solid oxide fuel cell (SOFC) has attracted considerable attention because of its unique advantages, such as high efficiency, environmental-friendly operations, and flexible fuels [1-4]. Currently, hydrogen gas is the most commonly used fuel for SOFCs, but its liquefaction temperature is too low (-253 ℃) for convenient transportation and storage, and it is rather expensive to produce [5, 6]. Therefore, the application of carbon fuels, such as methane, ethane, propane, syngas, and even solid carbon, is the ultimate goal of SOFC development [7-11].

Traditional nickel-based cermet anodes exhibit high electrical conductivity and good catalytic activity for electrochemical oxidation of hydrogen. Unfortunately, the inevitable coke deposition on these anodes when using carbon fuels may lead to rapid performance degradation which results from the coverage of electrochemical reaction sites by coke and nickel grain growth [11-14]. In recent years, novel SOFC stacks are being developed to work at lower temperatures to reduce the system cost and improve the system durability [15]. However, according to thermodynamic laws, coke formation is more severe at lower temperatures. Over the past decade, researchers have explored numerous alternative approaches to improve the carbon tolerance of Ni-based cermet anodes, such as alloying, doping Ni with noble metals, infiltrating the anodes with oxides, and reforming a catalyst layer. However, few of them can be applied practically due to several limiting factors, e.g. poor activity or high cost. In this case, novel anode materials and practical strategies to minimize coke deposition are critical for SOFCs

using carbon fuels [16].

Recently, perovskite oxides with flexible phase structures have been studied extensively, and they are reported to show great catalytic properties and stability when catalyzing less humid hydrocarbon fuels with suitable metal ions doped in A or B sites [17, 18]. Some single perovskite oxides, e.g. $La_{0.6}Sr_{0.4}VO_3$ (LSV) [19], $La_{1-x}Sr_xCr_{1-x}Fe_xO_{3-\delta}$ (LSCrF) [20], and $La_{0.75}Sr_{0.25}Cr_{0.5}Mn_{0.5}O_{3-\delta}$ (LSCM) [21], as well as double perovskite oxides like $Sr_2Fe_{1.5}Mo_{0.5}O_{6-\delta}$ (SFM) [22] and $PrBaMn_2O_{5+\delta}$ (PBM) [23], have been developed as anode materials. However, these materials alone are unsatisfactory when catalyzing the oxidation of hydrogen and carbon fuels.

To deal with such a problem, Ruddlesden-Popper (RP) layered perovskites with a K_2NiF_4-like structure have received much attention as the potential alternatives because they can hold a large amount of interstitial oxygen, resulting in high oxygen vacancy concentration, fast surface exchange, and the mixed transport of ions and electrons [24]. For example, Du and co-workers developed a nanocomposite anode made of primarily $FeNi_3$ bimetallic alloy. The anode was decorated with nanoparticles of Ruddlesden-Popper layered perovskite $Sr_3FeMoO_{7-\delta}$ and single perovskite $Sr(FeMo)O_{3-\delta}$, which were obtained by reducing the double perovskite $Sr_2FeMo_{0.65}Ni_{0.35}O_{6-\delta}$ (SFMNi) in H_2 at 850 ℃. The anode showed good electrochemical oxidation activity and coking tolerance in wet CH_4 [25]. However, the operating temperatures of these studies were quite high (800-900 ℃) because the catalytic activities for carbon fuels are insufficient

at intermediate temperatures.

It is interesting to note that alkali carbonates, especially Li_2CO_3 and K_2CO_3, have been widely used in direct carbon fuel cells (DCFCs), a derivative of SOFC with solid carbon as the fuel, as excellent catalysts for solid carbon fuel gasification [26, 27]. Rehman and co-workers partially substituted Sr in $SrFe_{0.8}Nb_{0.1}Ta_{0.1}O_{3-\delta}$ (SFNT) with Li and K, and they found that the product material showed higher concentrations of oxygen vacancy or electrical conductivity. Moreover, after CO_2 treatment, the formation of Li\K carbonates was verified by XPS, and these carbonates can significantly improve the catalyst's overall chemical stability and tolerance toward CO_2 poisoning [28]. In addition, lithium carbonate (melting point: 723 ℃) tends to be a liquid during cell operation, granting it high oxygen ion conductivity and facilitating better oxygen transfer. However, alkali carbonates have rarely been used to design anode materials with excellent catalytic activity and stability under an atmosphere of carbon fuels.

Inspired by previous researches on DCFCs, we proposed and evaluated a novel SOFC anode made by reducing $La_{0.65}Li_{0.05}Sr_{0.3}Fe_{0.8}Ni_{0.2}O_{3-\delta}$ ($LLSFN_{0.05}$). By detailed physicochemical and electrochemical tests, the impacts of Li dopant on the catalytic activity and catalyst stability were revealed. In addition, a reduced $LLSFN_{0.05}$ anode was exposed to a carbon fuel atmosphere, and Li_2CO_3 was found to form on the anode surface in-situ after reacting with CO_2, which could effectively gasify any solid carbon residues and enhance the anode's coking resistance. Furthermore, a single cell

demonstrated peak power densities (PPDs) of 467 mW cm^{-2} and 424 mW cm^{-2}, as well as satisfactory service lives of 80 h and 40 h, when CO and wet C_2H_6 were used as fuels, respectively. These data can be attributed to high catalytic activity, good coke-resistance, and excellent adhesion among the different phases in the reduced $LLSFN_{0.05}$.

2. Experimental procedure

2.1. Anode preparation

$La_{0.7-x}Li_xSr_{0.3}Fe_{0.8}Ni_{0.2}O_{3-\delta}$ (LLSFNx, x=0, 0.05, 0.1) powders were prepared via EDTA-citrate combustion. Briefly, nitrate precursors (Aladdin Chemical Reagent, China) of perovskite oxides were dissolved in deionized water, followed by the addition of citric acid and EDTA, as well as ammonia to adjust pH. An excessive amount of lithium nitrate was added to compensate for the volatilization of the alkali components in LLSFNx (x=0.05, 0.1). Stir the solution until it turned a sol-gel-like appearance, and dry the gel in an oven at 180 ℃ for 5 hours to get a black precursor. Subsequently, the precursor was calcinated at 550 ℃ for 4 h in the air to remove carbon. Then the remaining solid was ground and pressed into pellets, followed by sintering at 1050 ℃ for 10 h in the air to produce the LLSFNx powders. It should be noted when we attempted to sinter the precursor in air at 1000 ℃ for 5 h directly, we observed severe Li evaporation by testing the element content via inductively coupled plasma optical emission spectrometer (ICP-OES, Agilent 720ES). Reduced LLSFNx powders were obtained by treating LLSFNx in 10 vol.% H_2 (balanced with N_2) at 750 ℃ for 10 hours.

2.2. Property characterization

The crystallinity of the samples was detected via room-temperature X-ray diffraction (RT-XRD, Bruker AXS D8 Advance A25X). The metal content was examined via ICP-OES. The phase compositions, space groups, and lattice parameters were analyzed via Rietveld refinement using FullProf software. The morphology of the powders and single SOFCs was observed by scanning electron microscopy (SEM, FEI Inspect F50, USA). The morphology of the phase components was observed by high-resolution TEM (HR-TEM, FEI Tecnai G2 F20) and energy-dispersive X-ray spectroscopy (EDX). The valence states were determined based on X-ray photoelectron spectroscopy (XPS, Thermo Scientific K-Alpha) results. Silver wires and paste were used as conductive collectors.

Reduced LLSFNx powders were treated in 50% vol. CO (balanced with N_2) at 750 ℃ for 5 hours to observe their coking resistance. Their Raman spectra (Horiba Evolution) were measured at an excitation wavelength of 532 nm. O_2 temperature-programmed oxidation (O_2-TPO, AutoChem1 II 2920) of the powders was performed with a U-type quartz reactor at an oxygen flow rate of 20 mL min^{-1} and a heating rate of 10 ℃ min^{-1}. The amount of CO_2 generated by oxidizing the coke was measured based on the TCD signals.

2.3. Cell fabrication

A single experimental cell can be described as LLSFNx-SDC|SDC|LSFC-SDC. An SDC electrolyte pellet was produced by pressing 0.2 g SDC powders (Fuel Cell, USA) and subsequent calcination at 1300 ℃ for 10 hours. LSFC (Fuel Cell, USA) and SDC

powders were mixed in the isopropyl alcohol at a ratio of 7:3 to produce the cathode slurry, which was sprayed on one side of the SDC pellet. A similar procedure was used to produce anode slurry by mixing LLSFNx and SDC powders (with a weight ratio of 7:3), and the anode slurry was sprayed on the other side of the SDC pellet. Then the three-layered pellet was co-fired at 900 ℃ for 2 hours to obtain a single experimental fuel cell. The silver paste was brushed on the electrodes in a net shape for electron collection. Finally, the single cell was fixed on a quartz tube by the silver paste.

2.4. Electrochemical test

The cell's electrochemical performance was tested by a Solartron 1287 Electrochemical Workstation. The voltage amplitude was set as 30 mV and the frequency range was 0.1 Hz to 100 kHz in the electrochemical impedance spectra tests.

3. Results and discussions

3.1. Phase structure and microstructure

Phase structures of the prepared materials were first tested by RT-XRD (Fig. S1). It can be inferred from Fig. S1 that LSFN exhibits a single-phase perovskite structure, which is consistent with previous reports. The $LLSFN_{0.05}$ and $LLSFN_{0.10}$ samples contain some NiO phases (JCPDS#00-001-1239) with peaks at 37.4° and 43.5°, indicating that the samples are dual-phase composites. As shown in Table 1, the metal ions concentrations ratio tested by ICP-OES are similar with the metal ions stoichiometric ratio. The Li ion concentration is 2.15% which is lower than the Li ion stoichiometric ratio (2.5%), indicating there is a small amount of lithium deficiency caused by

volatilization. After reduction at 750 ℃ for 10 h in 10 vol.% H_2 (balanced with Ar), all the samples exhibit a multiphase composite structure, including the main phase of orthorhombic perovskite (O-LLSFN, space group: Pbnm), the second phase of RP-layered tetragonal perovskite (RP-LLSFN, space group: I4/mmm) and a minor phase of FeNi alloy (Fig. 1). As the Li concentration rises, the main peak of the perovskite phase shifts to a lower degree, implying lattice expansion. Such a phenomenon could result from the formation of oxygen vacancies and greater numbers of low-valence metal cations (Fig. 1b) [29]. Besides, the peak of SrO at 35.7 ° is clearly observed in the spectrum of reduced $LLSFN_{0.10}$, indicating structural decomposition in the perovskite with such a composition. Rietveld refinement results revealed that the content of RP-LLSFN is positively correlated with Li content (Fig. 1c, S2). The fitting parameters of R_{wp}, R_p, and χ^2 suggest a reliable fitting of the three composites [30]. It should be noted that the peak of FeNi alloy was removed from the Rietveld refinement analysis to prevent interference with the fitting of perovskite phase profiles.

The morphology of the reduced LLSFNx samples was investigated via SEM (Fig. S3, a-c). All three samples exhibit a homogeneous structure with uniformly distributed nanoparticles, suggesting successful exsolution of the nanoparticles from perovskite lattices. In addition, needle-like structures are seen on the reduced $LLSFN_{0.10}$, which is primarily due to perovskite decomposition.

Table 1. ICP-OES analysis of $La_{0.65}Sr_{0.3}Li_{0.05}Fe_{0.8}Ni_{0.2}O_3$ sample

Elements	La	Sr	Li	Fe	Ni
Metal ions concentration ratio	26. 72	17.00	2.15	43.52	10.61
Metal ions stoichiometric ratio	32.50	15.00	2.50	40.00	10.00

To further investigate the phase distributions in the reduced $LLSFN_{0.05}$ composite, we first exploited the microstructural and elemental distributions. The STEM image (Fig. 1d) reveals that some nanoparticles with a size of 35 nm are anchored on the grain surface. Besides, three diffraction planes with crystal spacings of 0.124 nm, 0.192 nm, and 0.116 nm were captured via high-resolution transmission electron microscopy (HR-TEM), which corresponds to O-LLSFN, RP-LLSFN, and FeNi alloy, respectively (Fig. 1e). Judging from Fig. 1e, the three phases are closely connected without any crack. Point EDX scanning reveals that Fe and Ni elements did not exsolve thoroughly and the perovskite parent maintained a stable phase structure (Fig. 1f). According to bright-field STEM and EDX mapping results (Fig. 1g), the nanoparticles attached on the surface of primary particles are predominantly made of Fe and Ni elements, suggesting the formation of FeNi alloy. All the elements (O, La, Fe, Ni, Sr) are homogeneously distributed, indicating good uniformity of the synthesized powders. It is well known that doped LLSFN and RP-LLSFN are mixed with oxygen ion and electron conductors while FeNi nanoparticles can enhance the surface catalytic activity [31]. Therefore, the $LLSFN_{0.05}$ nanocomposite can be a potential candidate for high-performance anodes in SOFCs.

XPS observations were performed to examine the surface chemistry of Fe and O in the samples. In pristine samples, the iron ions exhibit several distinct oxidation states at binding energies of 709.4 and 722.2 eV for Fe^{2+}, 710.7 and 724.0 eV for Fe^{3+}, and 714.0 and 726.9 eV for Fe^{4+}, respectively (Fig. 1h, S4) [32, 33]. Table S1 summarizes the percentages of Fe ions. The average valence of surface Fe decreases slightly as Li content rises. This is because Li exhibits lower electronegativity and replaces a small amount of La, resulting in denser electron clouds around the Fe atoms and lower average cation valence in Fe oxides [34]. After the reduction with H_2, a new peak of Fe^0 at 706 eV appeared in the reduced samples, suggesting successful exsolution of Fe. This result is in accordance with the TEM results, which state that the partial reduction of Fe ions comes from the perovskite lattice.

Besides, the reduction treatment reduces the average oxidation state from +3.07 to +2.87 for $LLSFN_{0.05}$. Two peaks at 531.7 eV and 528.6 eV are observed on the O 1s spectra, which correspond to lattice oxygen ($O_{lattice}$) and absorbed oxy gen ($O_{adsorbed}$), respectively [35]. $O_{adsorbed}$ species, such as OH^- and absorbed molecular H_2O, are associated with oxygen vacancies [36]. Based on the fitting peak areas, the $O_{adsorbed}$ contents of LSFN, $LLSFN_{0.05}$, and $LLSFN_{0.10}$ are calculated as 62.85%, 65.02%, and 66.11%, respectively (Fig. 1i, S5). Further, iodometric titration and TGA tests were conducted to measure the evolution of oxygen vacancies for LLSFNx (x=0, 0.05, 0.10) at 200–800 °C as shown in Fig. S6. According to the titration result, the oxygen vacancies concentrations of LSFN, $LLSFN_{0.05}$ and $LLSFN_{0.1}$ are 0.3, 0.33, and 0.34,

respectively, which is consistent with the XPS result. The oxygen non-stoichiometry in $LLSFN_{0.05}$ and LLSFN0.1 are always larger than that in LSFN up to 800 °C. It should be noted that the ionic radius of Li^{+}(VIII) is 0.92 Å, which is significantly smaller than that of Sr^{2+}(XII, 1.44Å) and La^{3+}(XII, 1.36Å). The size mismatch tends to lead Li dopants to migrate to the material surface and create A-site deficiency in the bulk, which is beneficial to the formation of oxygen vacancies. Hence, greater oxygen vacancies are generated to compensate the charge imbalance and A-site deficiency for size mismatch as a result of higher Li doping ratio. After reduction at a high temperature, the proportion of $O_{adsorbed}$ contents in $LLSFN_{0.05}$ increases to 88.71 % (Table S2). It should be noted that the surface oxygen species are intermediates of further oxidation, so higher Li concentrations and the partial transformation into RP phase perovskites work together to promote the capacity of oxygen ion transport, thereby boosting the catalytic activity for fuel oxidation [17].

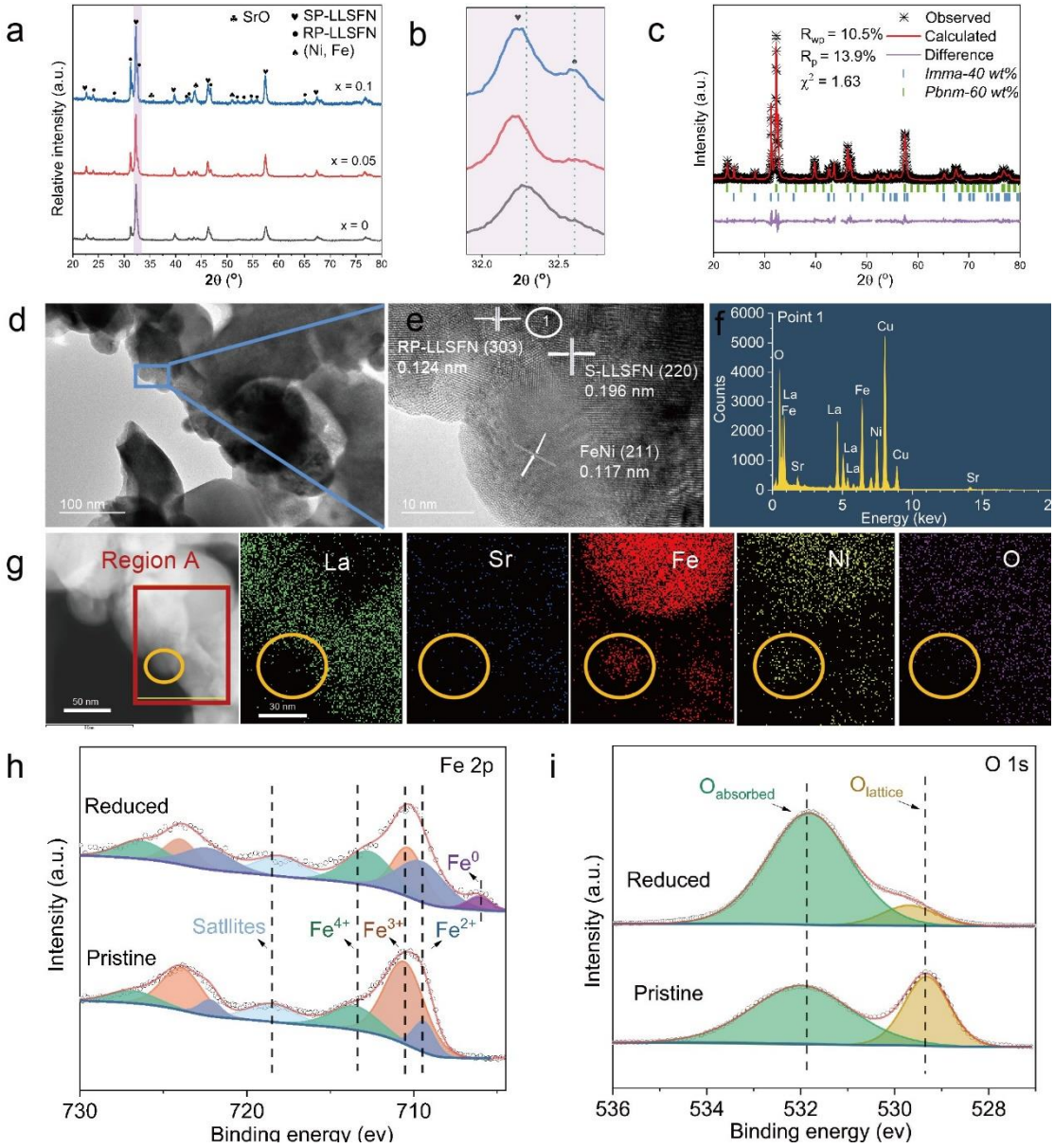

Fig. 1. a) Room-temperature XRD patterns of reduced LLSFNx (x = 0, 0.05, 0.10) powders in the air; b) The magnified spectra of a) between 31-33°; c) The refined XRD profiles of reduced $LLSFN_{0.05}$. d) STEM image, e) HR-TEM images, f) point EDX scanning results, and g) STEM-EDX mapping of the LLSFN0.05 sample. h) Fe 2p,+ i) O 1s XPS spectra of the as-prepared and reduced $LLSFN_{0.05}$.

3.2. Resistance toward carbon deposition

The positive role of Li dopant in removing carbon is described in Fig. 4. O_2-TPO and

Raman spectra experiments were performed on reduced LSFN and $LLSFN_{0.05}$ powders after they were exposed to a 50% vol. CO (balanced by N_2) atmosphere at 750 ℃ for 300 mins. Two Raman characteristic peaks associated with coke (C-C) are observed at 1580 cm^{-1} (G-band) and 1350 cm^{-1} (D-band) in both sample powders (Fig. 2a) [37]. The G-band reflects in-plane vibrations of carbon atoms, while the D-band originates from the structural disorder of coke. A larger peak intensity ratio $I_{(D)}/I_{(G)}$ suggests a lower degree of carbon graphitization [38], and the $I_{(D)}/I_{(G)}$ numbers of the carbon deposited on LSFN and $LLSFN_{0.05}$ are about 0.92 and 1.52, respectively, indicating that $LLSFN_{0.05}$ has a larger proportion of disordered carbon. Therefore, $LLSFN_{0.05}$ is more resistant to coking than LSFN.

Besides, a Raman signal located at 1060 cm^{-1} reveals carbonate formation in $LLSFN_{0.05}$ because of the high alkalinity of Li, but such a peak is not found for LSFN [39]. Consistent with previous findings that Li-doped perovskite could generate carbonates at the surface by CO_2 neutralization, this phenomenon may be due to the in-situ formation of lithium carbonate under the CO_2 atmosphere via the Boudouard reaction [28]. Fig. 2b depicts the O_2-TPO test results. Sasaki et al. drew several C-H-O phase diagrams to describe the compositions of the fuel system and pointed out the regions where carbon depositions appear at different temperatures [40]. Specifically, carbon depositions are inevitable if the reaction happens under a dry CO atmosphere at 750 ℃, which could explain the CO_2 peaks in both samples. However, as Li dopant promotes carbon removal, $LLSFN_{0.05}$ reveals a smaller peak area, and such an effect is amplified

in normal cell operations, where CO_2 is generated via CO oxidation.

In order to investigate the microstructure of $LLSFN_{0.05}$ powders after long-term service, we simulated the actual working conditions by treating the powder with a mixture of CO and CO_2 (8:2, mol/mol) for 300 mins, and the TEM images of the $LLSFN_{0.05}$ sample before and after CO/CO_2 treatment are obtained (Fig. 2c & d). Before the CO/CO_2 treatment, many FeNi nanoparticles are anchored on the body. However, after the treatment, smaller nanoparticles start to form. The yellow and red rings on the TEM images are used to distinguish the two different sizes of nanoparticles, where yellow rings indicate larger particles (~35 nm) and red rings indicate smaller ones (~10 nm). Subsequently, STEM was performed to observe the microstructures of both nanoparticles (Fig. 2e & f). Four diffraction planes with crystal spacings of 0.207 nm, 0.253 nm, 0.160 nm, and 0.126 nm were captured via HR-TEM, which correspond to (011), (010), and (111) diffraction planes of FeNi alloy and (331) of Li_2CO_3, respectively. CO is a weak reductant compared to hydrogen, which may explain why FeNi alloy nanoparticles show different sizes. Moreover, Li_2CO_3 content is also observed and verified as an effective catalyst for carbon gasification [41, 42]. No obvious coke deposition is observed on the TEM images, suggesting the effectiveness of Li dopant to remove coke via Boudouard reaction.

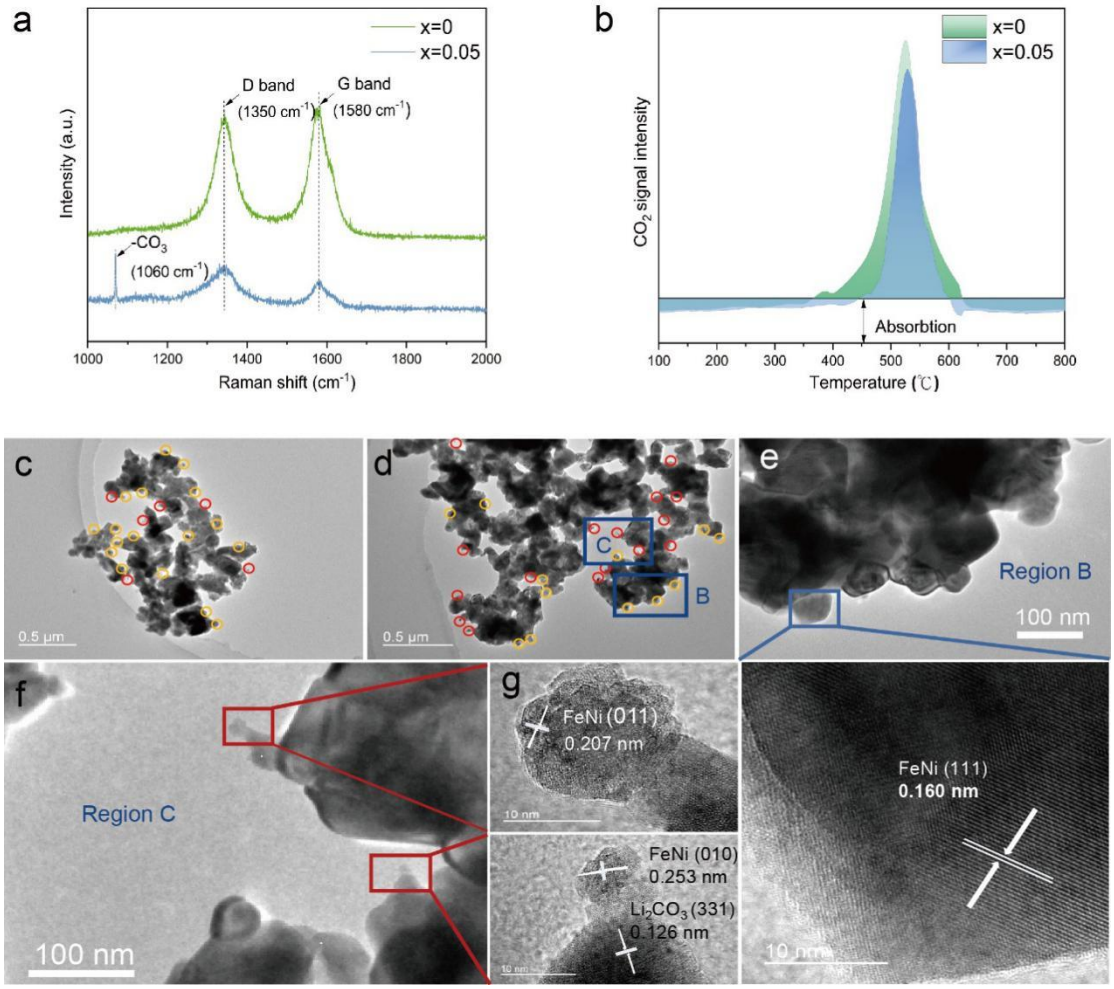

Fig. 2. a) Raman spectra and b) O_2-TPO curves of LSFN and $LLSFN_{0.05}$ after exposure in 50% vol. CO (balanced by N_2) at 750 ℃ for 5 h. c) & d) TEM images of the reduced $LLSFN_{0.05}$ sample before (c)) and after (d)) being exposed in the mixture of CO/N_2; e-f) STEM images and g) HR-TEM images of the $LLSFN_{0.05}$ sample after being exposed in the mixture of CO/CO_2 (8:2, mol/mol).

3.3. Electrochemical performance of single button cell using different fuels.

The electrochemical performance of the LLSFNx (x=0, 0.05, 0.1) anodes was assessed in SDC electrolyte-supported single cells. The cross-section morphology of the single cells was observed via SEM (Fig. S7). The thicknesses of $LLSFN_{0.05}$/SDC anode and SDC electrolyte are ~17 and ~250 μm, respectively. Firstly, the single cells' I-V curves

and their corresponding EIS spectra were measured at 750 ℃ with H_2 as the fuel. The Ohmic resistance of the electrolyte is subtracted from the impedance spectra to evaluate the Li-doping effects on electrode polarization. The peak power densities of the $LLSFN_{0.05}$ are calculated as 596 mW cm^{-2} (Fig. 3a), which is higher than LSFN (542 mW cm^{-2}) and $LLSFN_{0.10}$ (576 mW cm^{-2}). In addition, the total polarization resistance (Rp) of $LLSFN_{0.05}$ is 0.016 Ω·cm^2 , which is lower than LSFN (0.035 Ω cm^2) and $LLSFN_{0.10}$ (0.019 Ω cm^2) (Fig. 3d, Table S3). The observed peak power density of $LLSFN_{0.05}$ is much lower than that of the recently reported anode as shown in Table 2. These numbers suggest that a small amount of Li dopant can significantly accelerate anode reactions because of higher oxygen vacancy and the consequent higher catalytic activity on the electro-oxidation of H_2. For $LLSFN_{0.10}$, the impurities from perovskite decomposition may inhibit charge transfer in the anode, resulting in less satisfactory electrochemical performance.

Moreover, the cells adopting an $LLSFN_{0.05}$/SDC anode exhibit a peak power density (PPD) of 432, 294, and 201 mW cm^{-2} when operating on H_2 fuel at 700, 650, and 600 °C, respectively (Fig. S8). The EIS results for such anode and fuel combination are 0.034, 0.076, 0.164 Ω·cm^2 at 750, 700, 650 °C, respectively. The polarization resistance of our new anode material is 0.016 Ω·cm^2, which is much lower than that of other cells using the same cathode and electrolyte materials and different anode materials, such as $(PrBa)_{0.95}Fe_{1.9-x}Ni_xMo_{0.1}O_{6-\delta}$ (0.028 Ω cm^{-2}). The PPDs in the present study are not very high because thick electrolyte pellets were used and the SDC electrolyte may show

electrical leakage. It can be expected that PPDs can be greatly enhanced if the electrolyte thickness is reduced, or if electronic conduction through the electrolyte is suppressed. Judging from the present study, $LLSFN_{0.05}$ demonstrates the significant enhancement effect of Li dopant on the electro-oxidation of H_2.

Fuel flexibility is a unique advantage of SOFCs. Aside from H_2, other carbon fuels can also be used in SOFCs. Further electrochemical tests of single SOFCs were conducted to investigate the performance of $LLSFN_{0.05}$/SDC anodes with CO as the fuel, and the results are displayed in Fig. 3b. It can be inferred from the figure that when CO was used as the fuel, the single cells could not produce electrochemical performances as good as they could with H_2, suggesting that CO is oxidized at a lower rate than H_2. The cell with an $LLSFN_{0.05}$/SDC anode achieved the highest PPD of 467 mW cm^{-2} and the lowest total polarization resistance of 0.048 $\Omega \cdot cm^2$ among all the experimental cells (Fig. 3e, Table S3), which could be attributed to good coking resistance of $LLSFN_{0.05}$. When the tests were performed at a lower temperature, $LLSFN_{0.05}$/SDC cells still exhibit good PPDs of 311, 200, and 110 mW cm^{-2} and low polarization resistances of 0.075, 0.182, and 0.533 $\Omega \cdot cm^2$ at 700, 650, and 600 °C, respectively (Fig. S9), demonstrating significantly better electrochemical performances compared with other advanced anode materials such as $(PrBa)_{0.95}Fe_{1.4}Cu_{0.4}Nb_{0.2}O_{5+\delta}$ (417 mW/cm^{-2} at 800 °C) [43]. Hence, $LLSFN_{0.05}$ renders significantly better catalytic activities and coking resistance thanks to Li doping, thereby promoting the electrical performance of single cells.

Furthermore, the electrochemical performance of the $LLSFN_{0.05}$/SDC cell was measured under wet C_2H_6 at 750 °C (Fig. 3c & f). The cell demonstrates a PPD of 424, 240, 133, and 60 mW cm^{-2} and a polarization resistance of 0.028, 0.094, 0.373, and 1.608 Ω·cm^2 at 750, 700, 650, and 600 °C, respectively. Compared with the situation where CO is used as the fuel, cells fueled by wet C_2H_6 are more sensitive to the operation temperature, which could be explained as C_2H_6 cracking, from which H_2 can be generated, is more intense at higher temperatures.

Finally, the discharging curves of the LSFN/SDC and $LLSFN_{0.05}$/SDC cells using either CO or wet C_2H_6 as the fuel were obtained (Fig. 3g & 3h). For the $LLSFN_{0.05}$/SDC cells fueled by CO, they could endure the long-term stable durability test for 80 h without significant degradation, demonstrating good coking resistance (Fig. 3g). On the other hand, the cells $LLSFN_{0.05}$/SDC fueled by wet C_2H_6 maintained a continuous and stable operation for 40 h at a constant current density of 300 mA·cm^{-2} (Fig. 3h). In contrast, the total stable discharging time of the LSFN/SDC cells fueled by CO and C_2H_6 were only 40 and 9 h, respectively. The rapid degaradtion of the LSFN/SDC cells is mainly due to carbon deposition generated from the carbon fuels, covering the active reaction sites of anodes. It is noteworthy that there is a significant increase in voltage in the beginning, which may be attributed to the dynamic equilibrium between C_2H_6 cracking and reforming reactions and the consequent variations of gas composition in the anode chamber. Further, the durability test of the $LLSFN_{0.05}$/SDC cell under C_2H_6 was also

conducted as shown in Fig. S10. The total stable disacharging time of it is only 25 hours due to its instability under the reduced atmosphere.

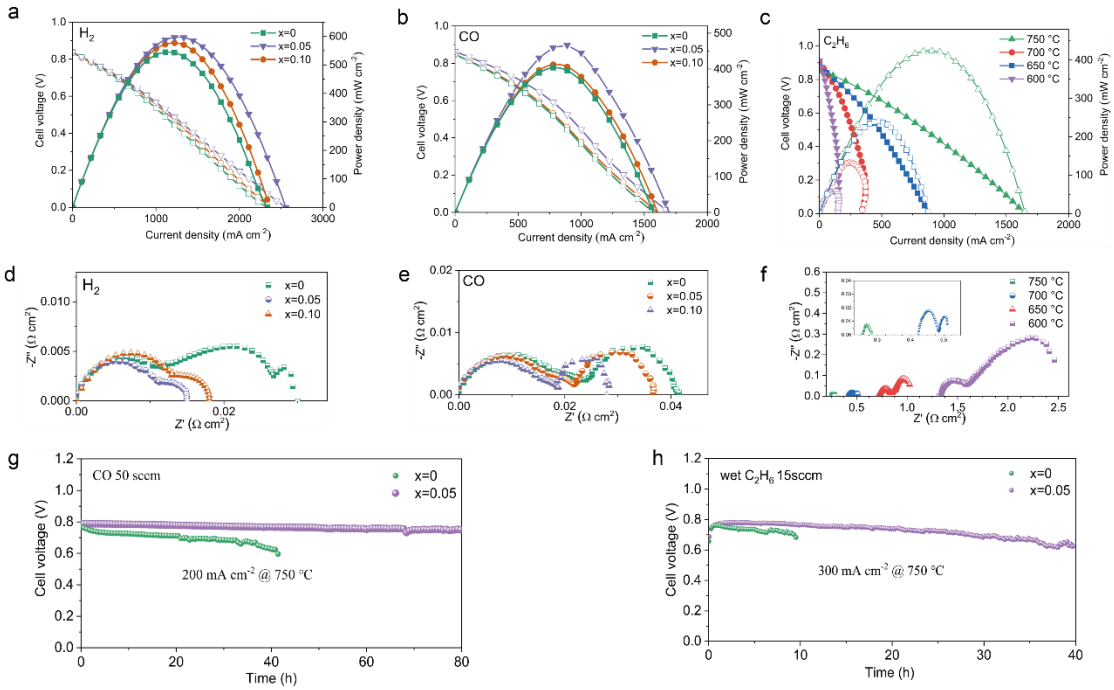

Fig. 3. I–V, I–P curves, and EIS spectra of SOFCs with different anodes operated on a, c) H_2 and b, d) CO fuels at 750 °C. e) I–V, I–P curves, and f) EIS spectra of SOFCs with an $LLSFN_{0.05}$-SDC anode operated on C_2H_6. Durability diagrams of a single cell with an $LLSFN_{0.05}$ anode fueled with g) dry CO and h) wet C_2H_6 at 750 °C.

Table 2 Summary of P_{max} and R_p values for different SOFC anode materials in H_2.

Anode	Electrolyte (μm)	Temperature (°C)	P_{max} (mW cm^{-2})	Ref.
$La_{0.52}Sr_{0.28}Ti_{0.94}Ni_{0.03}Co_{0.03}O_{3-\delta}$ infiltrated SDC	SDC (350)	800	479	[5]
$Sr_2FeMo_{0.65}Ni_{0.35}O_{6-\delta}$	$La_{0.9}Sr_{0.1}Ga_{0.8}Mg_{0.2}O_3$	750	590	[25]

	(300)			
$La_{0.7}Sr_{0.3}Fe_{0.9}Ni_{0.1}O_{3-\delta}$	$La_{0.9}Sr_{0.1}Ga_{0.8}Mg_{0.2}O_3$ (300)	750	400	[44]
$Pr_{0.6}Sr_{0.4}Fe_{0.7}Ni_{0.2}Mo_{0.1}O_{3-\delta}$	$La_{0.9}Sr_{0.1}Ga_{0.8}Mg_{0.2}O_3$ (300)	800	500	[45]
$(PrBa)_{0.95}Fe_{1.9-x}Ni_xMo_{0.1}O_{6-\delta}$-SDC	SDC (200)	750	588	[46]
$La_{0.65}Li_{0.05}Sr_{0.3}Fe_{0.8}Ni_{0.2}O_{3-\delta}$-SDC	SDC (250)	750	596	This work

3.4. Insight into the enhanced coke-resistance mechanism

The unique anode microstructures resulting from the in-situ formation of Li_2CO_3 in the presence of CO_2 are formed because at the surface, Li is a highly alkaline element (Fig. 4a). The ionic radius of Li^+ is dramatically smaller than Sr^{2+} and La^{3+}, which may render the migration of alkali dopants to the material surface and result in A-site deficiency in the bulk. The size mismatch and charge imbalance boost oxygen vacancies in alkali-doped anodes. The two carbon deposition reactions in our cell configuration (Fig. 10b) can be described as a CO disproportionation reaction (Eq. (1)) and a C_2H_6 cracking reaction (Eq. (2)).

$$2CO = C + CO_2 \quad (1)$$

$$C_2H_6 = 2C + 3H_2 \quad (2)$$

The process of carbon removal on the anode surface (Fig. 4c) includes the direct

electrochemical oxidation of CO and C_2H_6 by O^{2-} from electrolyte (Eq. (3)), the adsorption of CO_2 onto the Li_2CO_3 (Eq. (4)), and the reverse Boudouard reaction (Eq. (5)).

$$CO + O^{2-} = CO_2 + 2e^- \quad (3)$$

$$C_2H_6 + 7O^{2-} = 2CO_2 + 3H_2O + 14e^- \quad (4)$$

$$C + CO_2 = 2CO \quad (5)$$

In this study, Li_2CO_3 is demonstrated to adsorb CO_2 molecules. On the other hand, the mixed ionic-electronic conductors of RP-LLSFN and O-LLSFN ensure a rapid supply of oxygen ions to increase the electrochemical oxidation rate, generating sufficient CO_2 for further reactions. Besides, both Li_2CO_3 and FeNi alloy have a strong catalytic effect on carbon gasification. They could serve as surface-intermediate species in carbon removal by the reverse Boudouard reaction.

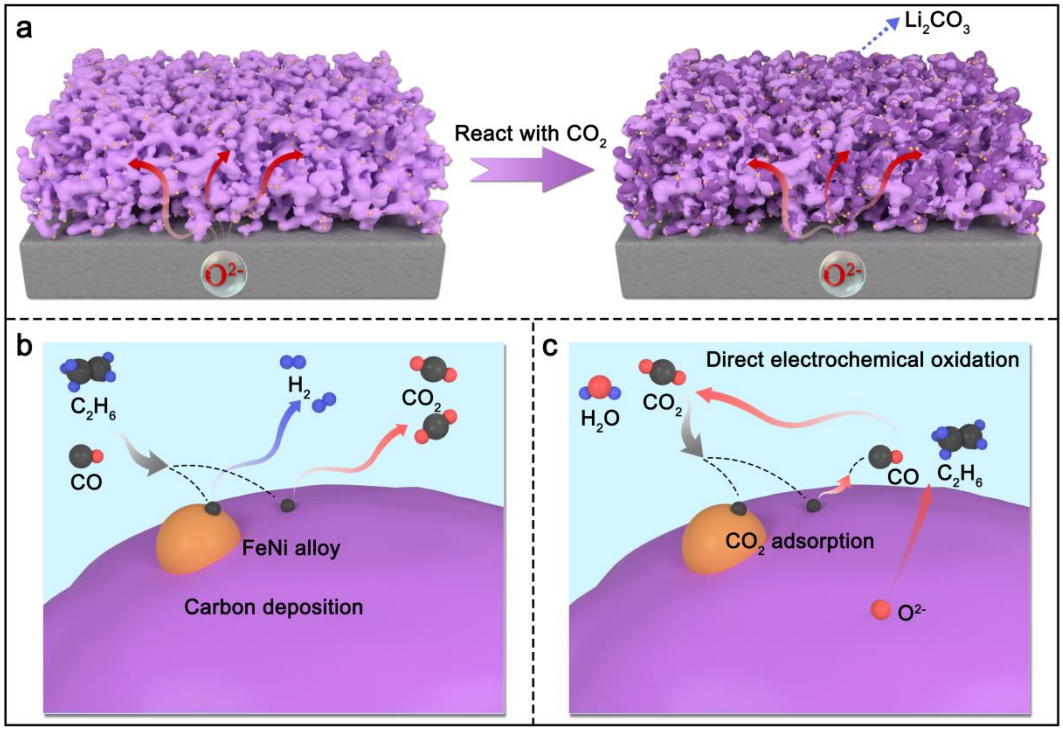

Fig. 4. a) A schematic illustration of in-situ carbonate formation in Li-doped LSFN

materials with a CO_2 atmosphere; b) carbon deposition in CO disproportionation and C_2H_6 cracking reactions; c) the proposed carbon-tolerant mechanism.

4. Conclusion

In summary, we proposed a novel multi-phase nanocomposite anode produced via one-step self-assembly reduction of $La_{0.65}Li_{0.05}Sr_{0.3}Fe_{0.8}Ni_{0.2}O_{3-\delta}$. This tightly assembled nanocomposite electrode is composed of a single perovskite main phase and an RP second phase with FeNi nanoparticles decorated on its surface. As for the electrochemical oxidation activity, the RP phase and Li dopant are found to enhance oxygen bulk diffusion, and FeNi alloy nanoparticles are verified to promote the overall catalytic activity. Additionally, the coking resistance of the proposed anode material under an atmosphere of 50% CO (balanced by N_2) is improved by doping Li. Moreover, attractive PPDs and stable operation periods at 750 ℃were achieved with the proposed cells. Finally, a novel mechanism of carbonate in-situ formation is proposed to explain the enhanced carbon tolerance of anodes, which could be of reference value to develop efficient and environmentally friendly applications of carbon fuel for CO_2 electrolysis.

Acknowledgments

This work was supported by Sichuan Science and Technology Department (Grant No. 2020YFH0012), National Natural Science Foundation of China Project (Grant No. 51827901, No. 52006150), Project of Strategic Importance Program of The Hong Kong Polytechnic University (Project ID: P0035168). We also thank Program for Guangdong

Introducing Innovative and Entrepreneurial Teams (Grant No. 2019ZT08G315), Natural Science Foundation of Guangdong Province (No. 2020A1515010550), Shenzhen Clean Energy Research Institute for support and Ceshigo Research for help in characterizations.

References

[1] Y.-H. Huang, R.I. Dass, Z.-L. Xing, J.B. Goodenough, Double perovskites as anode materials for solid-oxide fuel cells, Science 312(5771) (2006) 254-257.
[2] E.D. Wachsman, K.T. Lee, Lowering the temperature of solid oxide fuel cells, Science 334(6058) (2011) 935-939.
[3] M. Ni, Z. Shao, Fuel cells that operate at 300° to 500° C, Science 369(6500) (2020) 138-139.
[4] H. Xie, S. Zhai, T. Liu, H. Liao, Y. Zhang, W. Zhou, Z. Shao, M. Ni, B. Chen, Cu-modified Ni foams as three-dimensional outer anodes for high-performance hybrid direct coal fuel cells, Chemical Engineering Journal 410 (2021) 128239.
[5] Y. Song, H. Li, M. Xu, G. Yang, W. Wang, R. Ran, W. Zhou, Z. Shao, Infiltrated NiCo Alloy Nanoparticle Decorated Perovskite Oxide: A Highly Active, Stable, and Antisintering Anode for Direct‐Ammonia Solid Oxide Fuel Cells, Small 16(28) (2020) 2001859.
[6] J. Yang, A.F.S. Molouk, T. Okanishi, H. Muroyama, T. Matsui, K. Eguchi, Electrochemical and catalytic properties of Ni/BaCe0. 75Y0. 25O3− δ anode for direct ammonia-fueled solid oxide fuel cells, ACS applied materials & interfaces 7(13) (2015) 7406-7412.
[7] H. Su, Y.H. Hu, Progress in low-temperature solid oxide fuel cells with hydrocarbon fuels, Chemical Engineering Journal (2020) 126235.
[8] Y. Chen, Y. Zhang, Y. Lin, Z. Yang, D. Su, M. Han, F. Chen, Direct-methane solid oxide fuel cells with hierarchically porous Ni-based anode deposited with nanocatalyst layer, Nano Energy 10 (2014) 1-9.
[9] R. Deja, R. Peters, L. Blum, Methane/steam global reforming kinetics over the Ni/YSZ of planar pre-reformers for SOFC systems, Chemical Engineering Journal 292 (2016) 113-122.
[10] W. Bian, W. Wu, C.J. Orme, H. Ding, M. Zhou, D. Ding, Dual 3D Ceramic Textile Electrodes: Fast Kinetics for Carbon Oxidation Reaction and Oxygen Reduction Reaction in Direct Carbon Fuel Cells at Reduced Temperatures, Advanced Functional Materials 30(19) (2020) 1910096.
[11] W. Wang, C. Su, Y. Wu, R. Ran, Z. Shao, Progress in solid oxide fuel cells with nickel-based anodes operating on methane and related fuels, Chemical reviews 113(10) (2013) 8104-8151.
[12] Y. Chung, H. Kim, H. Yoon, J. Chung, N. Sammes, Effects of manganese oxide addition on coking behavior of Ni/YSZ anodes for SOFCs, Fuel Cells 15(2) (2015) 416-426.
[13] Y. Chen, B. deGlee, Y. Tang, Z. Wang, B. Zhao, Y. Wei, L. Zhang, S. Yoo, K. Pei, J.H. Kim, A robust fuel cell operated on nearly dry methane at 500° C enabled by synergistic thermal catalysis and electrocatalysis, Nature Energy 3(12) (2018) 1042-1050.
[14] Y. Wang, C. Wu, Q. Du, M. Ni, K. Jiao, B. Zu, Morphology and performance evolution of anode microstructure in solid oxide fuel cell: A model-based quantitative analysis, Applications in Energy and Combustion Science 5 (2021) 100016.

[15] D. Larrain, D. Favrat, Simulation of SOFC stack and repeat elements including interconnect degradation and anode reoxidation risk, Journal of Power Sources 161(1) (2006) 392-403.
[16] K. Wei, X. Wang, R.A. Budiman, J. Kang, B. Lin, F. Zhou, Y. Ling, Progress in Ni-based anode materials for direct hydrocarbon solid oxide fuel cells, Journal of materials science 53(12) (2018) 8747-8765.
[17] J. Li, J. Hou, X. Xi, Y. Lu, M. Li, Y. Fan, L. Wang, L. Wang, X.-Z. Fu, J.-L. Luo, Cogeneration of ethylene and electricity in symmetrical protonic solid oxide fuel cells based on a La 0.6 Sr 0.4 Fe 0.8 Nb 0.1 Cu 0.1 O 3− δ electrode, Journal of Materials Chemistry A 8(48) (2020) 25978-25985.
[18] C. Su, W. Wang, Z. Shao, Cation-Deficient Perovskites for Clean Energy Conversion, Accounts of Materials Research 2(7) (2021) 477-488.
[19] Z. Cheng, S. Zha, L. Aguilar, D. Wang, J. Winnick, M. Liu, A solid oxide fuel cell running on H2S／CH4 fuel mixtures, Electrochemical and Solid State Letters 9(1) (2005) A31.
[20] D.E. Fowler, J.M. Haag, C. Boland, D.M. Bierschenk, S.A. Barnett, K.R. Poeppelmeier, Stable, low polarization resistance solid oxide fuel cell anodes: La1–x sr x cr1–x fe x o3-δ (x= 0.2–0.67), Chemistry of Materials 26(10) (2014) 3113-3120.
[21] S. Tao, J.T. Irvine, A redox-stable efficient anode for solid-oxide fuel cells, Nature materials 2(5) (2003) 320-323.
[22] J. Feng, G. Yang, N. Dai, Z. Wang, W. Sun, D. Rooney, J. Qiao, K. Sun, Investigation into the effect of Fe-site substitution on the performance of Sr 2 Fe 1.5 Mo 0.5 O 6− δ anodes for SOFCs, Journal of Materials Chemistry A 2(41) (2014) 17628-17634.
[23] S. Sengodan, S. Choi, A. Jun, T.H. Shin, Y.-W. Ju, H.Y. Jeong, J. Shin, J.T. Irvine, G. Kim, Layered oxygen-deficient double perovskite as an efficient and stable anode for direct hydrocarbon solid oxide fuel cells, Nature materials 14(2) (2015) 205-209.
[24] C. Yang, J. Li, Y. Lin, J. Liu, F. Chen, M. Liu, In situ fabrication of CoFe alloy nanoparticles structured (Pr0. 4Sr0. 6) 3 (Fe0. 85Nb0. 15) 2O7 ceramic anode for direct hydrocarbon solid oxide fuel cells, Nano Energy 11 (2015) 704-710.
[25] Z. Du, H. Zhao, S. Yi, Q. Xia, Y. Gong, Y. Zhang, X. Cheng, Y. Li, L. Gu, K. Świerczek, High-performance anode material Sr2FeMo0. 65Ni0. 35O6− δ with in situ exsolved nanoparticle catalyst, ACS nano 10(9) (2016) 8660-8669.
[26] C. Jiang, J. Ma, A.D. Bonaccorso, J.T. Irvine, Demonstration of high power, direct conversion of waste-derived carbon in a hybrid direct carbon fuel cell, Energy & Environmental Science 5(5) (2012) 6973-6980.
[27] H. Xie, S. Zhai, B. Chen, T. Liu, Y. Zhang, M. Ni, Z. Shao, Coal pretreatment and Ag-infiltrated anode for high-performance hybrid direct coal fuel cell, Applied Energy 260 (2020) 114197.
[28] A.U. Rehman, M. Li, R. Knibbe, M.S. Khan, V.K. Peterson, H.E. Brand, Z. Li, W. Zhou, Z. Zhu, Enhancing oxygen reduction reaction activity and CO2 tolerance of cathode for low-temperature solid oxide fuel cells by in situ formation of carbonates, ACS applied materials & interfaces 11(30) (2019) 26909-26919.
[29] C. Xu, W. Sun, R. Ren, X. Yang, M. Ma, J. Qiao, Z. Wang, S. Zhen, K. Sun, A highly active and carbon-tolerant anode decorated with in situ grown cobalt nano-catalyst for intermediate-temperature solid oxide fuel cells, Applied Catalysis B: Environmental 282 (2021) 119553.
[30] Y. Song, Y. Chen, W. Wang, C. Zhou, Y. Zhong, G. Yang, W. Zhou, M. Liu, Z. Shao, Self-assembled triple-conducting nanocomposite as a superior protonic ceramic fuel cell cathode, Joule 3(11) (2019) 2842-2853.
[31] Y. Hou, L. Wang, L. Bian, N. Chen, K. Chou, High performance of Mo-doped La0. 6Sr0. 4Fe0. 9Ni0. 1O3-δ perovskites as anode for solid oxide fuel cells, Electrochimica Acta 292 (2018) 540-545.

[32] M.C. Biesinger, B.P. Payne, A.P. Grosvenor, L.W. Lau, A.R. Gerson, R.S.C. Smart, Resolving surface chemical states in XPS analysis of first row transition metals, oxides and hydroxides: Cr, Mn, Fe, Co and Ni, Applied Surface Science 257(7) (2011) 2717-2730.
[33] B.V. Crist, D.B. Crisst, Handbook of monochromatic XPS spectra, Wiley New York2000.
[34] A.U. Rehman, M. Li, R. Knibbe, M.S. Khan, W. Zhou, Z. Zhu, Unveiling Lithium Roles in Cobalt‐Free Cathodes for Efficient Oxygen Reduction Reaction below 600° C, ChemElectroChem 6(20) (2019) 5340-5348.
[35] S. Liu, Q. Liu, J.-L. Luo, The excellence of La (Sr) Fe (Ni) O 3 as an active and efficient cathode for direct CO 2 electrochemical reduction at elevated temperatures, Journal of Materials Chemistry A 5(6) (2017) 2673-2680.
[36] J. Zhao, X. Xu, W. Zhou, Z. Zhu, An in situ formed MnO‐Co composite catalyst layer over Ni–Ce 0.8 Sm 0.2 O 2− x anodes for direct methane solid oxide fuel cells, Journal of Materials Chemistry A 5(14) (2017) 6494-6503.
[37] H. Wu, J. Xiao, X. Zeng, X. Li, J. Yang, Y. Zou, S. Liu, P. Dong, Y. Zhang, J. Liu, A high performance direct carbon solid oxide fuel cell–A green pathway for brown coal utilization, Applied Energy 248 (2019) 679-687.
[38] Y. Jiao, L. Wang, L. Zhang, W. An, W. Wang, W. Zhou, M.O. Tadé, Z. Shao, J. Bai, S.-D. Li, Direct operation of solid oxide fuel cells on low-concentration oxygen-bearing coal-bed methane with high stability, Energy & Fuels 32(4) (2018) 4547-4558.
[39] R.L. Frost, M.L. Weier, J.T. Kloprogge, Raman spectroscopy of some natural hydrotalcites with sulphate and carbonate in the interlayer, Journal of Raman Spectroscopy 34(10) (2003) 760-768.
[40] K. Sasaki, Y. Teraoka, Equilibria in fuel cell gases: II. the CHO ternary diagrams, Journal of The Electrochemical Society 150(7) (2003) A885.
[41] N. Wu, W. Wang, Y. Zhong, G. Yang, J. Qu, Z. Shao, Nickel‐iron alloy nanoparticle‐decorated K2NiF4‐type oxide as an efficient and sulfur‐tolerant anode for solid oxide fuel cells, ChemElectroChem 4(9) (2017) 2378-2384.
[42] A. Fuente-Cuesta, C. Jiang, A. Arenillas, J.T. Irvine, Role of coal characteristics in the electrochemical behaviour of hybrid direct carbon fuel cells, Energy & Environmental Science 9(9) (2016) 2868-2880.
[43] M. Ma, J. Qiao, X. Yang, C. Xu, R. Ren, W. Sun, K. Sun, Z. Wang, Enhanced stability and catalytic activity on layered perovskite anode for high-performance hybrid direct carbon fuel cells, ACS applied materials & interfaces 12(11) (2020) 12938-12948.
[44] L. Bian, C. Duan, L. Wang, R. O'Hayre, J. Cheng, K.-C. Chou, Ce-doped La 0.7 Sr 0.3 Fe 0.9 Ni 0.1 O 3− δ as symmetrical electrodes for high performance direct hydrocarbon solid oxide fuel cells, Journal of Materials Chemistry A 5(29) (2017) 15253-15259.
[45] X. Lu, Y. Yang, Y. Ding, Y. Chen, Q. Gu, D. Tian, W. Yu, B. Lin, Mo-doped Pr0. 6Sr0. 4Fe0. 8Ni0. 2O3-δ as potential electrodes for intermediate-temperature symmetrical solid oxide fuel cells, Electrochimica Acta 227 (2017) 33-40.
[46] S. Xue, N. Shi, Y. Wan, Z. Xu, D. Huan, S. Zhang, C. Xia, R. Peng, Y. Lu, Novel carbon and sulfur-tolerant anode material FeNi 3@ PrBa (Fe, Ni) 1.9 Mo 0.1 O 5+ δ for intermediate temperature solid oxide fuel cells, Journal of Materials Chemistry A 7(38) (2019) 21783-21793.